SUPPLEMENTAL INFORMATION

Standalone Photo–Rechargeable Capacitor Integrating DSSCs with a Bi//$NiCo_2S_4$ Asymmetric Supercapacitor for High–Efficiency Indoor and Outdoor Energy Storage

Ying-Chu Chen[a], Ting-Ya Wu[b], Chih-Hung Tsai [b] and Yu-Kuei Hsu[b,]*

[a]*Department of Chemical Engineering & Biotechnology, National Taipei University of Technology, No. 1, Sec.3, Zhong-Xiao E. Rd., Da'an Dist., Taipei City 10608, Taiwan*

[b]*Department of Opto-Electronic Engineering, National Dong Hwa University, No. 1, Sec. 2, Da Hsueh Road, Shoufeng, Hualien, 97401, Taiwan*

*Corresponding author. Tel: +886-3-863-3196; Fax: +886-3-863-3180.

E-mail address: ykhsu@gms.ndhu.edu.tw

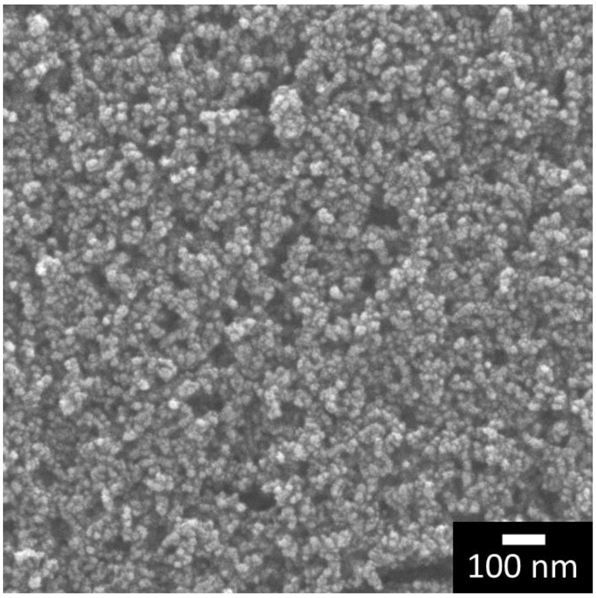

Figure S1. SEM image of the N719 dye–sensitized TiO_2 photoelectrode.

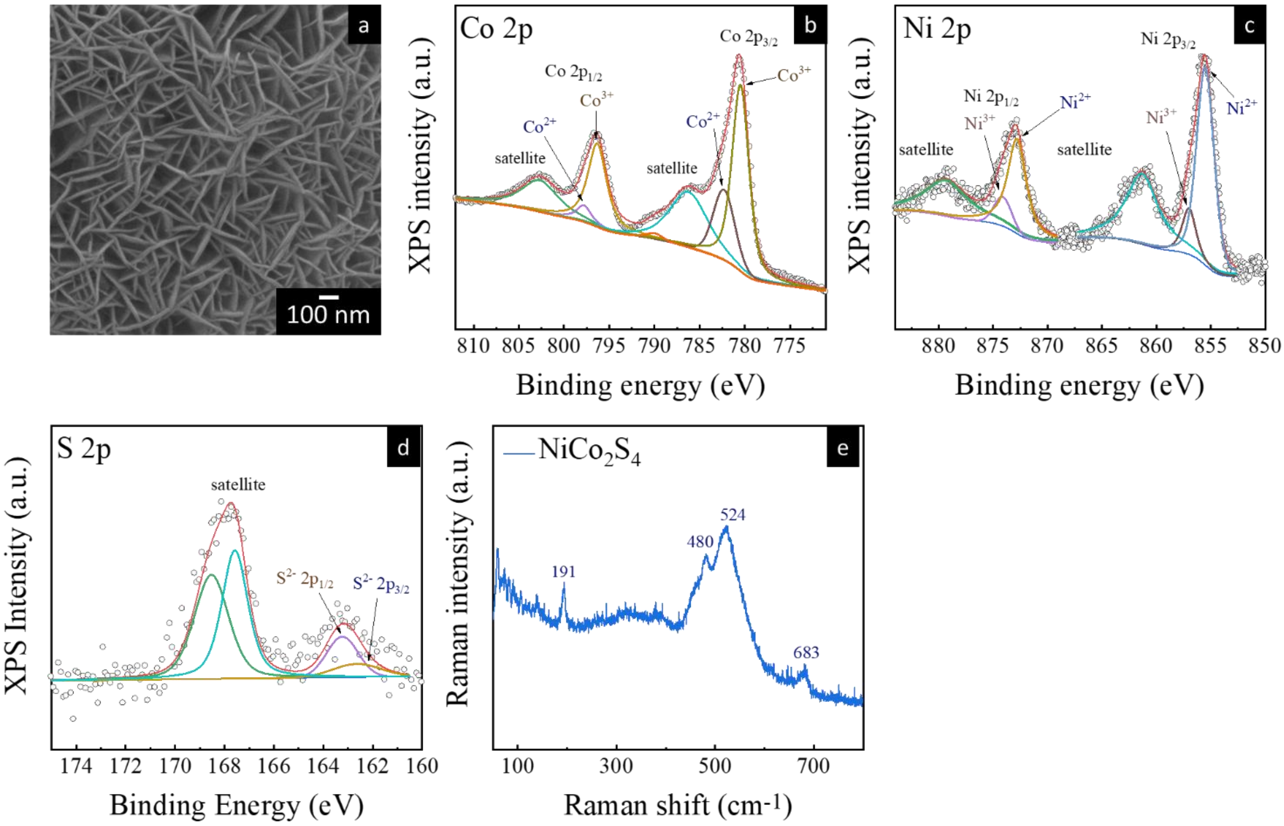

Figure S2. (a) SEM image, (b) Co 2*p*, (c) Ni 2*p*, (d) S 2*p* core–level XP spectra and (e) Raman spectrum of $NiCo_2S_4$ counter electrode.

The deconvolution of the Co 2*p* core–level XP spectrum of $NiCo_2S_4$ (Fig. S2b) yields four components at binding energy (B.E.) of 780.48 eV, 782.38 eV, 796.33 eV, and 797.88 eV, corresponding to the Co^{3+} $2p_{3/2}$, Co^{2+} $2p_{3/2}$, Co^{3+} $2p_{1/2}$ and Co^{2+} $2p_{1/2}$ emission lines, respectively. Notably, the relative intensities of the Co^{3+} $2p_{3/2}$ and $2p_{1/2}$ peaks are substantially higher than those of their Co^{2+} counterparts, indicating that Co^{3+} is the predominant oxidation state within $NiCo_2S_4$.

Similarly, deconvolution of the Ni 2*p* core–level XP spectrum (Fig. S2c) reveals four fitted components at B.E. values of 855.53 eV, 856.93 eV, 872.83 eV, and 874.18 eV, assigned to the Ni^{2+} $2p_{3/2}$, Ni^{3+} $2p_{3/2}$, Ni^{2+} $2p_{1/2}$ and Ni^{3+} $2p_{1/2}$ emission lines, respectively. The strong intensity of the Ni^{3+} $2p_{3/2}$ and $2p_{1/2}$

peaks confirms that Ni^{3+} is also abundant in $NiCo_2S_4$.

The S 2*p* core–level XP spectrum (Fig. S2d) is deconvoluted into four components at 162.63 eV, 163.23 eV, 167.58 eV, and 168.53 eV. The two lower–energy features are attributed to the S^{2-} $2p_{3/2}$ and S^{2-} $2p_{1/2}$ emission lines, whereas the higher–energy components are most likely associated with elemental sulfur (S^0) or polysulfide species (S_n^{2-}, $n \leq 2$) formed via surface oxidation of $NiCo_2S_4$ upon air exposure [1]. Although these oxidized sulfur species cannot be definitively assigned, they are not central to the present study.

Raman analysis (Fig. S2e) further supports this interpretation. All observed vibrational modes at 191 cm^{-1}, 480 cm^{-1}, 524 cm^{-1}, and 683 cm^{-1} are more consistent with the characteristic features of nickel cobalt oxide ($NiCo_2O_4$) rather than pristine $NiCo_2S_4$, suggesting that $NiCo_2S_4$ readily undergoes surface oxidation in atmosphere—a trend that is in excellent agreement with prior reports in the literature [2].

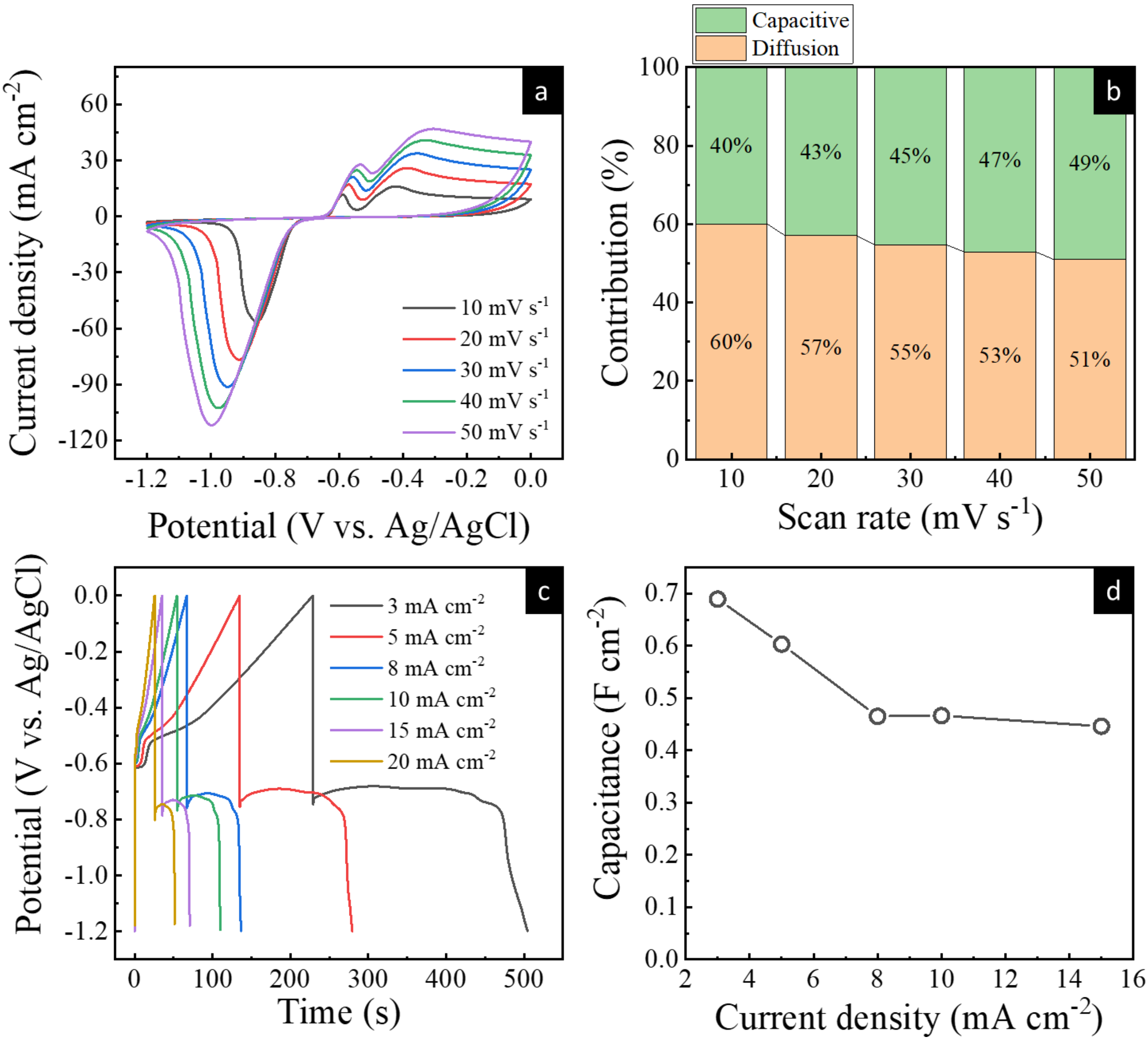

Figure S3. (a) CV curves of Bi storage electrode. (b) Capacitive and diffusion–controlled contributions to charge storage by Bi storage electrode. (c) GCD plots of Bi storage electrode. (d) Areal capacitance of Bi storage electrode as a function of current density.

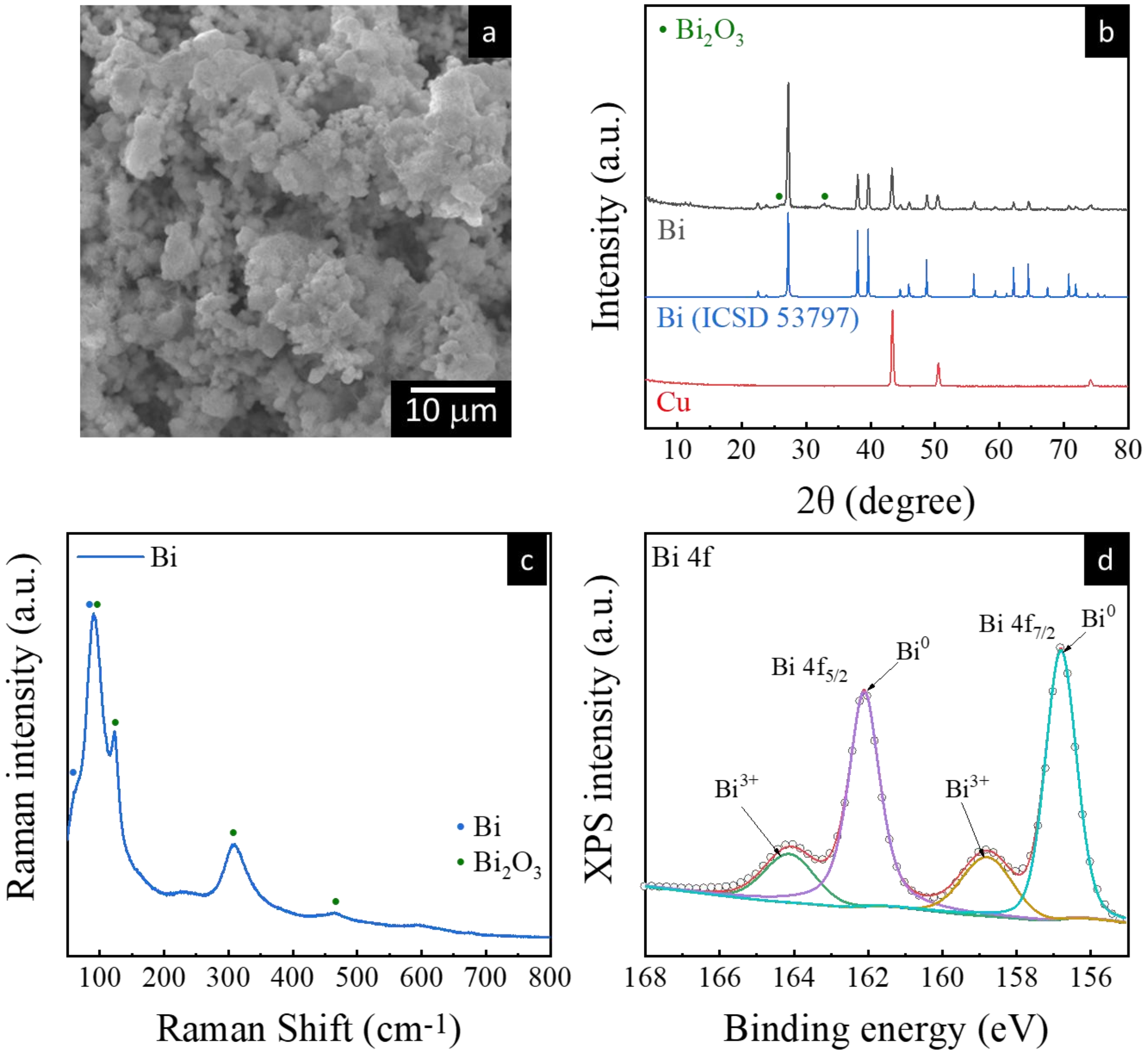

Figure S4. (a) SEM image, (b) XRD pattern, (c) Raman spectrum and (d) Bi 4*f* core–level XP spectrum of Bi storage electrode. XRD and powder diffraction patterns of Cu and Bi (ICSD 53797) are plotted alongside in (b) for comparison.

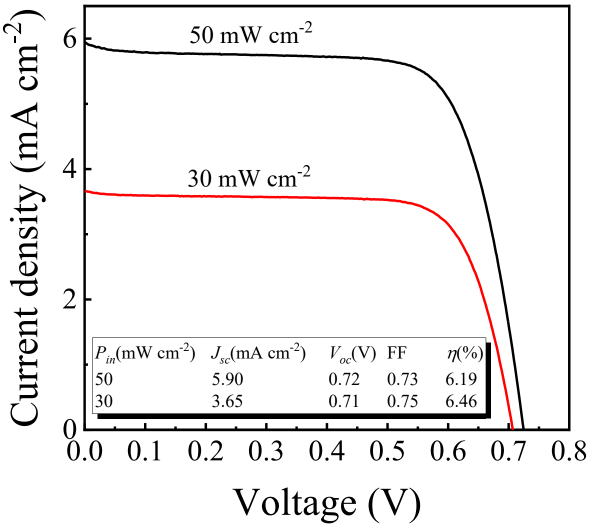

Figure S5. *J–V* curves of DSSC sensitized by N719 with Pt counter electrode under solar illumination with different light intensity. Inset: Summarized performance of DSSC (P_{in}: light intensity, FF: fill factor).

Supplementary Note S1. Carrier ions participating in the Faradaic reaction of the Bi charge storage electrode.

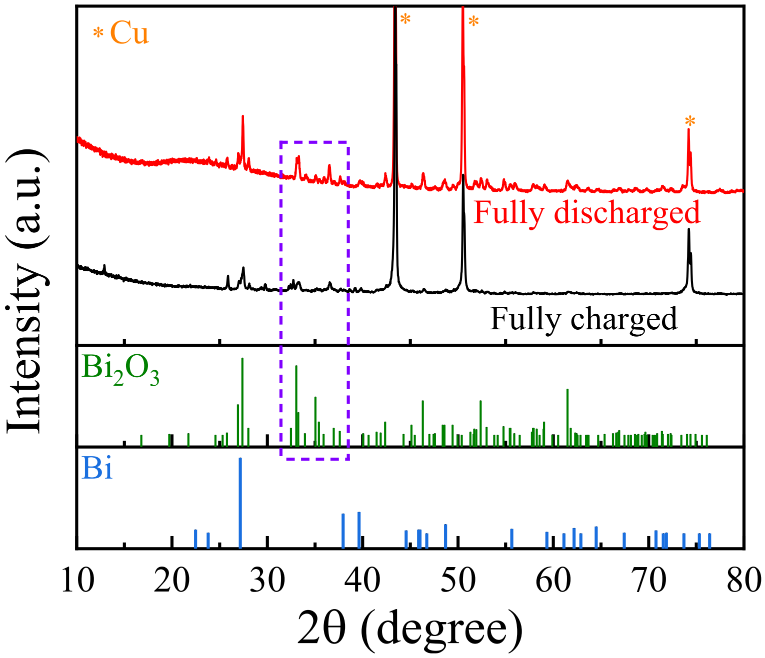

Figure S6. XRD patterns of Bi storage electrode at different charged and discharged states.

Fig. S6 summarized the XRD patterns collected for the Bi storage electrode at different charged states, wherein the characteristic bismuth oxide (Bi_2O_3) diffraction peaks, rather than potassium–bismuth (K–Bi) alloy phases are clearly observed. Upon charging, these oxide–related peaks are substantially attenuated, accompanied by the re–emergence of metallic Bi diffraction peaks, indicating a highly reversible redox process involving hydroxide ions (OH^-). These results demonstrate OH^- in lieu of potassium ion (K^+) is the carrier ions participating in the Faradaic reaction of the Bi charge storage electrode (Eqn. 10 in the main text).

Supplementary Note S2. Light–intensity–dependent photocharging kinetics.

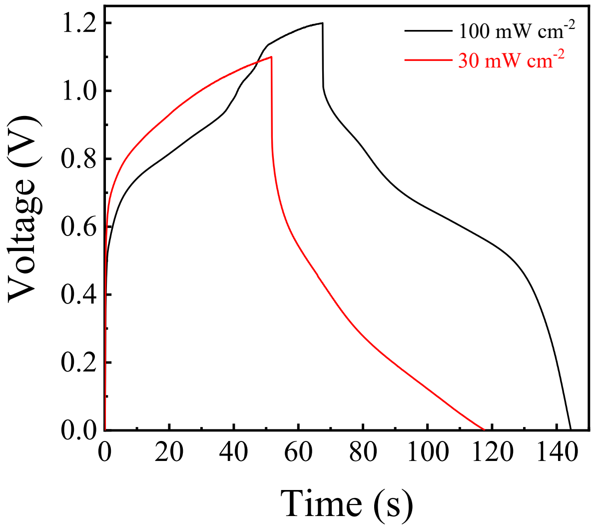

Figure S7. Photocharging of PC under solar illumination with different light intensity and galvanostatically discharging at a current density of 3 mA cm^{-2}.

Fig. S7 compares the photocharging and subsequent galvanostatic discharging behavior of the PC under solar illumination at different light intensities. As shown, the maximum cell voltage (V_{cell}) reached during photocharging decreases modestly from ~1.2 V under one–sun illumination (100 mW cm^{-2}) to ~1.1 V under dim–light conditions (30 mW cm^{-2}). This behavior directly reflects the light–intensity dependence of the DSSC component, whose open–l circuit voltage (V_{oc}) decreases slightly from ~0.74 V under one–sun illumination to ~0.71 V under reduced light intensity (Fig. S5).

Despite this reduction, the attained V_{cell} under dim–light illumination remains well above the minimum thermodynamic voltage (~0.81 V), estimated from the redox potentials of Bi (-0.46 V_{SHE}) and the I_3^-/I^- couple (0.35 V_{SHE}), required to activate the Faradaic reactions at both the Bi storage electrode and the I_3^-/I^- redox mediator. Consequently, effective photocharging of the PC is sustained under both illumination conditions, and the overall photocharging durations under one–sun and dim–light illumination remain comparable, as observed in Fig. S7.

Notably, the slightly lower V_{cell} attained under dim–light illumination leads to a higher discharge capacitance when the device is galvanostatically discharged at 3 mA cm^{-2} (Fig. 4c in the main text). Specifically, an areal capacitance of 180.82 mF cm^{-2} is obtained at 30 mW cm^{-2}, compared with 170.40 mF cm^{-2} under one–sun illumination. This enhancement, together with the improved photovoltaic conversion efficiency of DSSCs under low–light conditions (Fig. 1a in the main text and Fig. S5), collectively contributes to the higher overall energy–storage efficiency observed at reduced light intensity (Fig. 4d in the main text).

The difference in discharge capacitance under varying illumination conditions is closely associated with the photocurrent delivered by the DSSC (Fig. 1a and Fig. 4c in the main text, Fig. S5). Under dim–light illumination, the photocurrent density is substantially lower—approximately one–quarter of that under one–sun illumination—resulting in a slower photocharging process. This mild charging regime is kinetically favorable for OH^- ions and the I_3^-/I^- redox shuttle to diffuse and participate effectively in the Faradaic reactions at the Bi and $NiCo_2S_4$ electrodes. As a result, pseudocapacitive charge–storage processes dominate, as described by Eqn. 3-6 and Eqn. 10 in the main text.

This interpretation is supported by the comparable discharge durations observed under dim–light and one–sun illumination, despite the lower V_{cell} reached under the former condition (Fig. S7). In contrast, the higher photocurrent density under one–sun illumination accelerates the photocharging process, which limits ion diffusion and suppresses the full development of Faradaic reactions at the storage electrodes. Under these conditions, charge storage is dominated by electric double–layer capacitance (EDLC), which provides faster charge–discharge kinetics but a lower overall capacitance. This transition accounts for the superior rate capability of the PC under strong illumination relative to dim–light conditions (Fig. 4c in the main text).

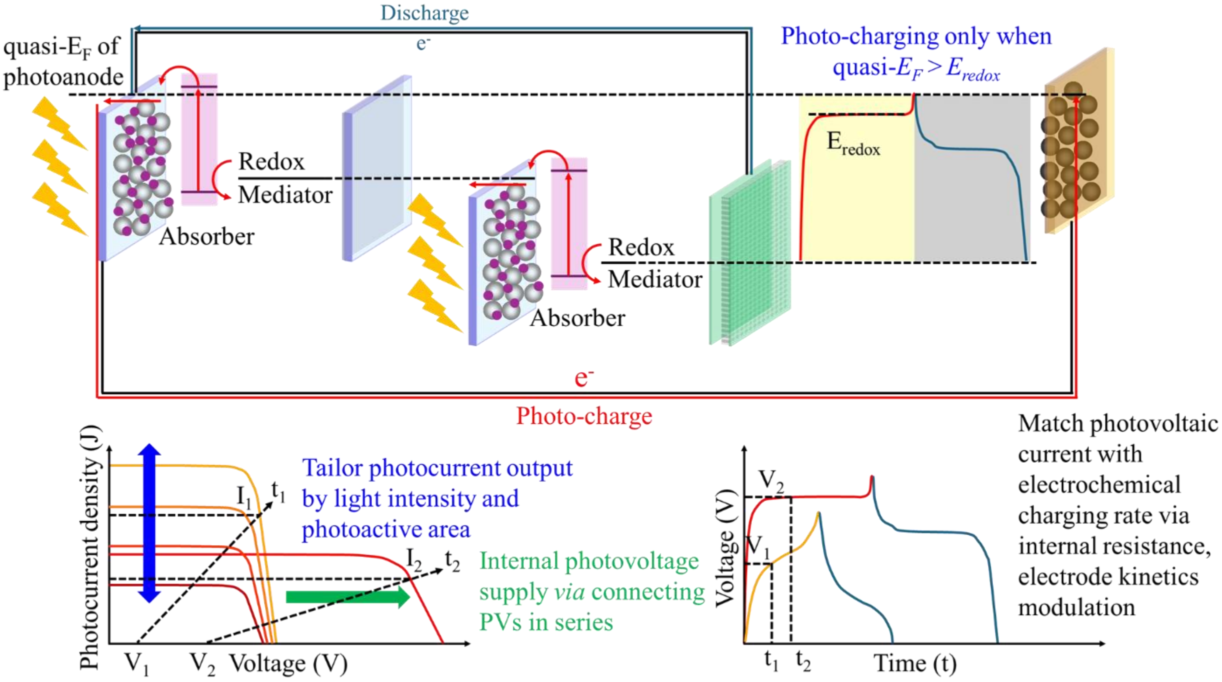

Scheme S1. General design principles for integrated photo–rechargeable energy storage systems. **(1)** Energetic alignment: photo–charging occurs only when the quasi–Fermi level (quasi–E_F) of photoexcited electrons under illumination lies above the redox (or intercalation) potential (E_{redox}) of the storage electrode (quasi–$E_F > E_{redox}$), enabling spontaneous electron transfer from the photovoltaic unit to the storage electrode. (2) Photovoltaic–electrochemical matching: the photocurrent generated by the photovoltaic component should be matched with the electrochemical charging characteristics of the storage device, which can be tuned through parameters such as light intensity and photoactive area. (3) Device–level optimization: efficient operation further requires balancing key device parameters, including solar–cell area, internal resistance, and electrode kinetics, together with providing sufficient internal photovoltage (e.g., via series connection of photovoltaic units) to drive the charging reactions. These factors collectively govern the photo–charging efficiency and overall performance of integrated photo–rechargeable capacitors.

Reference

[1] P. Büttner, F. Scheler, D. Döhler, M. K. S. Barr, M. Bosch, M. Rey, T. Yokosawa, S. Hinz, J. Maultzsch, E. Spiecker, N. Vogel, I. Mínguez-Bacho and J. Bachmann, *Nano Energy*, **2022**, *103*, 107820.

[2] C. Xia, P. Li, A. N. Gandi, U. Schwingenschlögl and H. N. Alshareef, *Chem. Mater.*, **2015**, *27*, 6482–6485.